

Equatorial Asymmetry of the East Pacific ITCZ: Observational Constraints on the Underlying Processes

HIROHIKO MASUNAGA

Hydrospheric Atmospheric Research Center, Nagoya University, Nagoya, Japan

TRISTAN S. L'ECUYER

Department of Atmospheric Science, Colorado State University, Fort Collins, Colorado

(Manuscript received 17 May 2010, in final form 13 November 2010)

ABSTRACT

The equatorial asymmetry of the east Pacific intertropical convergence zone (ITCZ) is explored on the basis of an ocean surface heat budget analysis carried out with a variety of satellite data products. The annual mean climatology of absorbed shortwave flux exhibits a pronounced meridional asymmetry due to a reduction of insolation by high clouds in the north ITCZ. Ocean mixed layer advection has the largest, if not exclusive, effect of counteracting this shortwave-exerted asymmetry. Other heat fluxes, in particular latent heat flux, predominate over the advective heat flux in magnitude but are secondary with respect to equatorial asymmetry. The asymmetry in advective heat flux stems from a warm pool off the Central American coast and, to a lesser extent, the North Equatorial Counter Current, neither of which exist in the Southern Hemisphere. The irregular continental geography presumably comes into play by generating a warm pool north of the equator and bringing cold waters to the south in the far eastern Pacific.

In addition to the annual climatology, the north–south contrast in the seasonal cycle of surface heat flux is instrumental in sustaining the north ITCZ throughout the year. The northeast Pacific is exposed to a seasonal cycle that is considerably weaker than that in the southeast Pacific, arising from multiple causes including the finite eccentricity of the earth's orbit and meridional gradient in mixed layer absorptivity. Simple experiments generating synthetic sea surface temperature (SST) illustrate that the muted seasonal cycle of heat flux forcing moderates the SST seasonal variability in the northeast Pacific and thus allows the north ITCZ to persist year round. Existing theories on the ITCZ asymmetry are briefly examined in light of the present findings.

1. Introduction

The equatorial asymmetry of the intertropical convergence zone (ITCZ) over the east Pacific Ocean has been extensively studied over past decades. A tight correlation of atmospheric dynamics with underlying sea surface temperature (SST), as well known from observations (Fig. 1), offer compelling evidence for the critical importance of air–sea interaction. Different hypotheses have been proposed to explain the ITCZ asymmetry in terms of air–sea interaction including the wind–evaporation–SST (WES) feedback (Xie and Philander 1994), stratus–SST feedback (Philander et al. 1996), and upwelling–SST feedback

(Mitchell and Wallace 1992; Chang and Philander 1994), as reviewed by Li (1997) and Xie (2004). The irregular continental geometry along the Central and South American coastlines arguably destroys the equatorial symmetry in addition to the processes internal to ocean–atmosphere dynamics (Philander et al. 1996; Xie and Saito 2001).

The ITCZ asymmetry has been studied principally by means of coupled ocean–atmosphere models at different levels of complexity. Simplified models are suited for efficiently tracking down critical physical processes, but the simplifications could filter out some processes that otherwise might be found crucial for giving rise to the asymmetry. Meanwhile, it remains a formidable task for state-of-the-art coupled climate models to simulate the east Pacific ITCZ precisely as observed (Mechoso et al. 1995; Dai 2006; de Szoeke and Xie 2008). Compared to this rich spectrum of modeling studies exploring the

Corresponding author address: Hirohiko Masunaga, Hydrospheric Atmospheric Research Center, Nagoya University, F3-1(200) Furocho Chikusa-ku, Nagoya 458-0015, Japan.
E-mail: masunaga@hyarc.nagoya-u.ac.jp

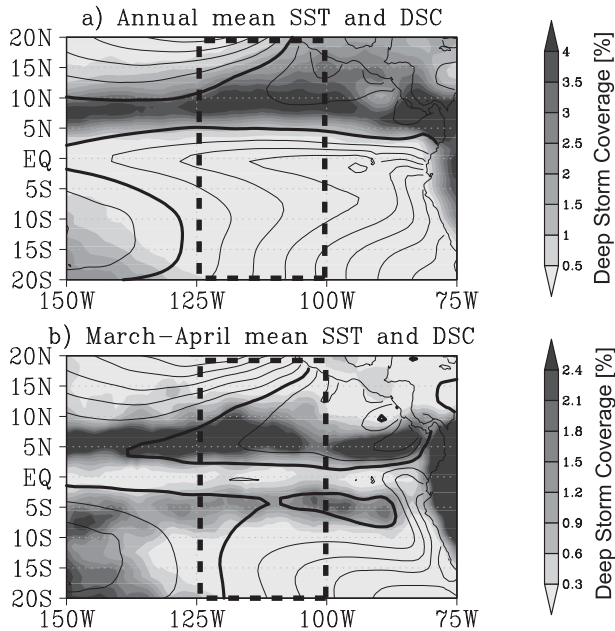


FIG. 1. (a) Geographical map of annual-mean deep storm coverage (shaded) and SST (contour). The contour interval is 1°C , and 27°C is highlighted by the thick line. The dashed box indicates the primary target area of the present analysis. (b) As in (a) but for March–April bimonthly mean.

ITCZ asymmetry, observational work against which proposed hypotheses can be tested in depth is rather limited. A notable exception is the East Pacific Investigation of Climate Processes in the Coupled Ocean–Atmosphere System 2001 (EPIC2001), a field campaign program targeted on interactive air–sea processes in the tropical east Pacific (Raymond et al. 2004). The present paper is intended to join efforts to fill in the lack of such observational benchmarks as well as to identify key processes possibly missing from the existing theories. To this end, the ocean mixed layer heat budget is analyzed with surface heat fluxes estimated primarily from a wide variety of satellite measurements.

The ocean surface heat budget has been studied extensively by combined in situ and satellite measurements over the equatorial Pacific (Wang and McPhaden 1999), the equatorial cold tongue (Swenson and Hansen 1999), the ITCZ–equatorial cold tongue complex (McPhaden et al. 2008), and the east Pacific warm pool (Wijesekera et al. 2005), among others. The current analysis relies on satellite data and ancillary global datasets and therefore does not attempt to quantitatively refine the previous heat budget estimates derived from buoy and ship observations. This work, instead, is aimed at analyzing the climatological large-scale structure of surface heat fluxes and ocean heat transport over the entire tropical east Pacific beyond the limited areal coverage observable by

in situ stations. Such an approach is required since the ITCZ asymmetry essentially involves large-scale air–sea dynamics.

In this work, the observed equatorial asymmetry of the east Pacific ITCZ is documented in terms of the estimated heat fluxes and underlying factors such as clouds, wind, and SST. Following an overview of the analysis strategy in section 2, the annual mean climatology is first presented (section 3) to outline the processes that potentially maintain the north–south asymmetry of the ITCZ. Factors responsible for the ITCZ asymmetry in the annual mean field are further examined in comparison with the seasonal double ITCZ observed in the March–April climatology (section 4). The persistence of the north ITCZ and the transience of the south ITCZ are then explored by analyzing the seasonal cycle of the surface heat fluxes in section 5. The present findings are discussed and concluded in section 6.

2. Data and method

a. Ocean heat flux estimate

The ocean mixed layer heat budget is analyzed with a variety of datasets based primarily on satellite measurements. The overall strategy follows Masunaga and L'Ecuyer (2010) but a number of modifications have been made to improve the fidelity of the model. The basic equation governing the mixed layer heat budget is

$$\rho_w H_{\text{ml}}(x, y) C_{p,w} \frac{\partial T_s(x, y, t)}{\partial t} = Q_{\text{net}}(x, y, t) - \langle Q_{\text{res}} \rangle(x, y). \quad (1)$$

The net heat flux, Q_{net} , is broken down into

$$Q_{\text{net}} = Q_{\text{adv}} + Q_{\text{upw}} + Q_{\text{SW}} + Q_{\text{LW}} + Q_{\text{LH}} + Q_{\text{SH}} + Q_{\text{dif}},$$

where Q_{adv} is the advective heat flux, Q_{upw} the upwelling heat flux, Q_{SW} the shortwave flux absorbed into the ocean mixed layer, Q_{LW} the longwave flux, Q_{LH} the latent heat flux, Q_{SH} the sensible heat flux, and Q_{dif} the diffusional heat flux. The residual term,

$$\langle Q_{\text{res}} \rangle(x, y) = \frac{1}{T} \oint Q_{\text{net}}(x, y, t) dt,$$

represents biases associated with the present estimates of individual heat fluxes. Here T represents one climatological year and the integral applies to the whole annual cycle. Methodology to derive individual heat fluxes is next reviewed.

1) LATENT AND SENSIBLE HEAT FLUXES

The latent heat flux through evaporation from the ocean surface is estimated by use of a bulk formula:

$$Q_{\text{LH}} = \rho_a L_v C_E [q_v - q_v^*(T_s)] |\mathbf{u}_{10}|, \quad (2)$$

where ρ_a , L_v , q_v , $q_v^*(T_s)$, and \mathbf{u}_{10} are the dry air density, vapor latent heat per unit mass, vapor mixing ratio, saturation vapor mixing ratio for SST or T_s , and wind velocity at 10 m above the sea surface, respectively. The bulk transfer coefficient for evaporation, C_E , is adopted from Large et al. (1994). In this study, T_s and \mathbf{u}_{10} are provided by the Tropical Rainfall Measuring Mission (TRMM) Microwave Imager (TMI) and the Quick Scatterometer (QuikSCAT) SeaWinds instrument, respectively, and q_v is related to TMI-retrieved column water vapor (CWV) through the water vapor scale height, H_v , as

$$\rho_a q_v = \text{CWV}/H_v, \quad (3)$$

where H_v is assumed to be a function of CWV and SST:

$$H_v = f(\text{CWV}, T_s). \quad (4)$$

Masunaga and L'Ecuyer (2010) found that H_v is well constrained by CWV and SST, and empirically defined a bivariate linear regression equation for (4) in comparison with moored buoy data. This linear formula is replaced in the present work by a tabulated database representing $f(\text{CWV}, T_s)$, constructed with the Atmospheric Infrared Sounder (AIRS) daily gridded product matched to CWV and SST from the Advanced Microwave Scanning Radiometer for the Earth Observing System (AMSR-E). The AIRS vapor mixing ratio in the lowermost atmospheric layer (1000–925 hPa) is extrapolated down to the surface using a simple boundary layer model, in which potential temperature and vapor mixing ratio are assumed to be constant within the atmospheric mixed layer and follow a moist adiabat above. The surface vapor mixing ratio, providing the lower boundary condition to this model, is evaluated so that the model temperature and humidity profiles are consistent with a given AIRS estimate. Simultaneous AIRS and AMSR-E measurements over the tropical east Pacific for five years from 1 January 2003 to 31 December 2007 are employed to build the lookup table of H_v .

The sensible heat flux, Q_{SH} , is taken from the Japanese Ocean Flux Datasets with Use of the Remote Sensing Observations 2 (J-OFURO2) dataset (Kubota et al. 2002).

2) OCEAN ADVECTION AND UPWELLING FLUXES

The advective heat flux is evaluated as

$$Q_{\text{adv}} = -C_{p,w} \rho_w H_{\text{ml}} \mathbf{u} \cdot \nabla T_s, \quad (5)$$

where $C_{p,w} = 4.0 \times 10^3 \text{ J kg}^{-1} \text{ K}^{-1}$ is the specific heat of ocean water, $\rho_w = 1030 \text{ kg m}^{-3}$ the ocean water density, \mathbf{u} the current velocity taken from the Ocean Surface Current Analysis–Real time (OSCAR) product (Bonjean and Lagerloef 2002), and H_{ml} is the mixed layer depth adopted from de Boyer Montégut et al. (2004).

The upwelling velocity, w_E , at the mixed layer bottom is

$$w_E = \frac{1}{\rho_w} (\nabla \cdot \mathbf{M}_{\text{ml}}), \quad (6)$$

where the mixed layer mass transport, \mathbf{M}_{ml} , is determined as follows. The conventional formulation of 1.5-layer models for tropical oceans implies

$$\mathbf{u}_m = \mathbf{u}_1 - \mathbf{u}_e \frac{H_{\text{tc}} - H_{\text{ml}}}{H_{\text{tc}}}, \quad (7)$$

where \mathbf{u}_m is the vertical mean current in the dynamically active layer, \mathbf{u}_1 is the surface current, and \mathbf{u}_e is the Ekman current or the shear between the mixed layer and underlying layer (e.g., Zebiak and Cane 1987; Chang 1994). The thermocline depth, H_{tc} , is approximated by the 20°C depth determined with the *World Ocean Atlas 2005 (WOA05)* (Locarnini et al. 2006). Equation (7) is rewritten in terms of mass transport as

$$\frac{H_{\text{ml}}}{H_{\text{tc}}} \mathbf{M} = \mathbf{M}_{\text{ml}} - \frac{H_{\text{tc}} - H_{\text{ml}}}{H_{\text{tc}}} \mathbf{M}_E, \quad (8)$$

where $\mathbf{M} \equiv H_{\text{tc}} \mathbf{u}_m$ is the total mass transport above the thermocline and $\mathbf{M}_E \equiv H_{\text{ml}} \mathbf{u}_e$ is the surface Ekman mass transport. Taking the divergence of (8), one obtains

$$\frac{H_{\text{ml}}}{H_{\text{tc}}} \nabla \cdot \mathbf{M} = \nabla \cdot \mathbf{M}_{\text{ml}} - \nabla \cdot \left(\mathbf{M}_E \frac{H_{\text{tc}} - H_{\text{ml}}}{H_{\text{tc}}} \right), \quad (9)$$

where $H_{\text{ml}}/H_{\text{tc}}$ is assumed not to be highly variable over distance. In (11), the lhs vanishes if $\nabla \cdot \mathbf{M}$ is negligibly small compared to individual terms on the rhs, that is, the active layer is nearly nondivergent as a whole. Combining (6) and (9) then leads to

$$w_E = \frac{1}{\rho_w} \nabla \cdot \left(\mathbf{M}_E \frac{H_{\text{tc}} - H_{\text{ml}}}{H_{\text{tc}}} \right). \quad (10)$$

The surface Ekman flow, $\mathbf{M}_E \equiv (M_{E,x}, M_{E,y})^T$, is evaluated from the observed wind stress field as

$$r_s M_{E,x} - f M_{E,y} = \tau_x \quad (11)$$

and

$$r_s M_{E,y} + f M_{E,x} = \tau_y, \quad (12)$$

where $r_s = 6.62 \times 10^{-6} \text{ s}^{-1}$ is the drag coefficient (Lagerloef et al. 1999), f is the Coriolis parameter, and τ_x and τ_y are the zonal and meridional components of the wind stress, respectively. The bulk formula by Large et al. (1994) is applied to the QuikSCAT wind vector to estimate τ_x and τ_y in (11) and (12). The upwelling (or entrainment) heat flux is then evaluated from w_E as

$$Q_{\text{upw}} = -\rho_w C_{p,w} W_e \mathcal{H}(W_e) \Delta T_E, \quad (13)$$

with the entrainment rate at the mixed layer base (Stevenson and Niiler 1983):

$$W_e = w_E + \mathbf{u} \cdot \nabla H_{\text{ml}},$$

where \mathcal{H} is the Heaviside function and ΔT_E represents the temperature difference between mixed layer water and upwelling water from beneath. In the entrainment rate, the Eulerian derivative term $\partial H_{\text{ml}}/\partial t$ has been omitted since H_{ml} is temporally fixed in the current analysis. The second term in W_e is minor, overall, compared to the upwelling velocity. In this work, ΔT_E is defined between the depths of $0.5H_{\text{ml}}$ and $H_{\text{ml}} + 15 \text{ m}$ using the *WOA05* temperature profile.

3) RADIATIVE FLUX

The downward shortwave and longwave fluxes at the bottom of the atmosphere (BOA), denoted $F_{\text{SW}}^{\downarrow}$ and $F_{\text{LW}}^{\downarrow}$ are provided by the Hydrologic Cycle and Earth Radiation Budget (HERB) product (L'Ecuyer and Stephens 2003, 2007; L'Ecuyer and McGarragh 2010). The net longwave heat flux at the surface is written as

$$Q_{\text{LW}} = (1 - \epsilon_s) F_{\text{LW}}^{\downarrow} - \epsilon_s \sigma T_s^4, \quad (14)$$

where $\sigma = 5.67 \times 10^{-8} \text{ W m}^{-2} \text{ K}^{-4}$ is the Stephan-Boltzmann constant and ϵ_s is the longwave surface emissivity. In this study, ϵ_s is fixed at unity (Kraus and Businger 1994; Large and Yeager 2009). The net shortwave flux absorbed by the ocean mixed layer is

$$Q_{\text{SW}} = (1 - \alpha) \Pi F_{\text{SW}}^{\downarrow}, \quad (15)$$

where α is the ocean surface albedo and Π is the fraction of incoming shortwave energy absorbed into the mixed layer. Ocean surface albedo is specified as a function of solar zenith angle using the spectral albedo model of Jin et al. (2004). For simplicity, Π is parameterized by a simple function of H_{ml} :

$$\Pi = (1 - \gamma) + \gamma \left[1 - \exp\left(-\frac{H_{\text{ml}}}{h_\gamma}\right) \right] = 1 - \gamma \exp\left(-\frac{H_{\text{ml}}}{h_\gamma}\right), \quad (16)$$

where $\gamma = 0.47$ is the fraction of solar flux that falls in the penetrative wave band (380–700 nm) and $h_\gamma = 20 \text{ m}$ is the depth scale for the penetration of insolation over this wave band (Murtugudde et al. 2002).

4) DIFFUSIONAL HEAT FLUXES

The ocean heat flux due to horizontal diffusion is

$$Q_{\text{dif}} = \rho_w C_{p,w} H_{\text{ml}} \kappa \nabla^2 T_s, \quad (17)$$

where the turbulent diffusion coefficient κ is conservatively chosen to be $3 \times 10^3 \text{ m}^2 \text{ s}^{-1}$ (e.g., Bauer et al. 1998). Vertical diffusion at the mixed layer base is not considered in the present analysis.

b. Data

TMI-retrieved SST and CWV datasets are provided by the Remote Sensing Systems (RSS), and \mathbf{u}_{10} is from the QuikSCAT L3 daily data product. Low and high cloud fractions analyzed in this paper are retrieved from TRMM TMI and Visible/Infrared Scanner (VIRS) measurements by the HERB algorithm and are, therefore, physically consistent with the radiative flux estimates. Precipitating portions of cloud systems are delineated by use of the TRMM Precipitation Radar (PR) echo-top height along with VIRS infrared brightness temperature (IR T_b) (Masunaga et al. 2005; Masunaga and Kummerow 2006). Vertically developed precipitating clouds, represented by the combination of the “deep stratiform” and “deep convective” classes in the Masunaga et al. (2005) terminology, are identified by PR echo tops higher than 4 km collocated with IR T_b colder than 245 K. The area fraction of such towering precipitating clouds is hereafter denoted by deep storm coverage and used as an indicator of deep convective activity. Note that the deep storm coverage only represents precipitating clouds while the HERB cloud fractions contain nonprecipitating clouds as well.

The whole dataset is analyzed on a $1^\circ \times 1^\circ$ Cartesian grid for eight years of observations from 1 January 2000 to 31 December 2007. The J-OFURO2 dataset is unavailable beyond 2006, so the sensible heat climatology is computed from seven years omitting 2007. All heat fluxes and atmospheric parameters studied are first evaluated on a daily basis and then averaged to climatology. Pentad time series of the OSCAR current is temporally interpolated to daily sequences. Ancillary parameters for characterizing the ocean interior, that is, H_{ml} , ΔT_E , and H_{tc} , are fixed at the annual mean field.

The primary study area is zonally bound by 125° and 100°W , chosen so that the analysis is targeted specifically on the east Pacific ITCZ. The south ITCZ, when it appears, would be contaminated with the easternmost portion of the

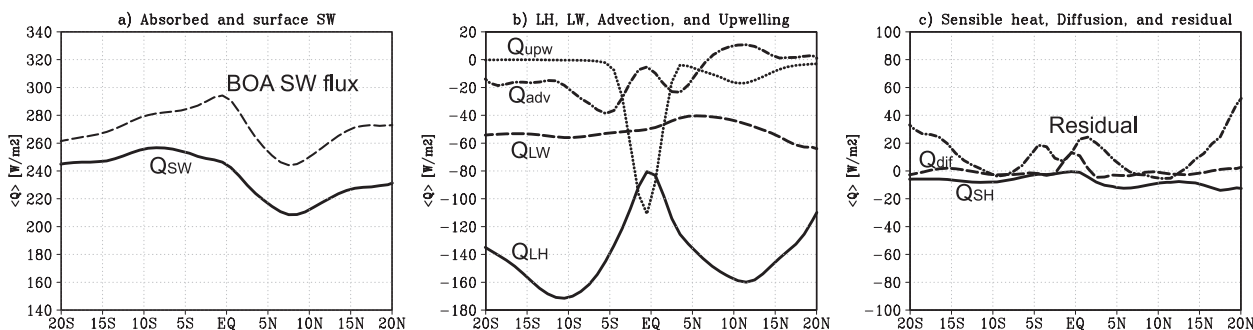


FIG. 2. Climatological zonal-mean heat fluxes averaged between 125° and 100°W . Despite having different intercepts, the vertical axis spans 200 W m^{-2} in all panels. (a) Total BOA shortwave flux (dashed) and that absorbed at the surface (Q_{SW} , solid). (b) Latent heat flux (Q_{LH} , solid), upwelling heat flux (Q_{upw} , dotted), longwave flux (Q_{LW} , dashed), and advective heat flux (Q_{adv} , dotted-dashed). (c) Sensible heat flux (Q_{SH} , solid), diffusion heat flux (Q_{dif} , dashed), and the residual term (dotted-dashed).

South Pacific convergence zone (SPCZ) if the western edge were extended beyond 125°W , while the eastern edge (100°W) of the study area is limited by a geographical constraint imposed by the Central American landmass (see Fig. 1). The sectors south and north of the equator dividing the study area are hereafter denoted by the southeast Pacific (SEP) and the northeast Pacific (NEP). In section 5, the SEP (NEP) is limited further to the meridional range of 15°S – 2°S (2°N – 15°S) for defining regional means, excluding the narrow equatorial band between 2°S and 2°N to avoid the equatorial cold tongue.

3. Annual mean climatology

The annual mean climatology of the east Pacific ITCZ is first examined focusing on the different factors contributing to the ocean heat budget.

a. Zonal-mean heat fluxes

Figure 2 shows the zonal-mean heat fluxes averaged from 125° to 100°W . The incoming shortwave flux at the BOA (dashed line in Fig. 2a) exhibits a remarkable meridional asymmetry, showing a distinct minimum around 5° – 10°N and a maximum at the equator. This equatorial asymmetry is preserved as the surface shortwave flux penetrates deeper and is absorbed in the ocean mixed layer, reaching a maximum difference of $\sim 40 \text{ W m}^{-2}$ between 10°S and 10°N (solid line in Fig. 2a). Since insolation at the top of the atmosphere is virtually symmetric about the equator when the seasonal cycle is averaged out, this north–south asymmetry results from unevenly distributed atmospheric and oceanic components that modulate the downwelling shortwave flux absorbed in the mixed layer, as will become clearer later.

The energy input by the absorbed shortwave flux must be locally balanced in the long-term mean with all other heat fluxes combined. Figure 2b illustrates major heat

fluxes counteracting the absorbed shortwave flux. The latent heat flux is predominant (i.e., largest in negative flux) except near the equator, where the upwelling cooling dominates the other terms. The latent heat flux is characterized by a pair of negative maxima near 10°S and 10°N with the southern maximum slightly exceeding its northern counterpart in negative magnitude. The longwave flux is relatively homogeneous across the study area. The advective heat flux, although minor in amplitude compared to the other fluxes plotted together, has a notable north–south contrast and even changes sign to positive for latitudes north of 7°N .

The remaining heat fluxes and residual term are depicted in Fig. 2c. The sensible and diffusion heat fluxes are minimal throughout the entire tropical latitudes. The residual term, $\langle Q_{\text{res}} \rangle$, exhibits an equatorially asymmetric twist in proximity of the equator (5°S – 5°N) but transitions into a roughly symmetric pattern as latitude increases farther poleward. The equatorial bias is likely attributed to errors in the upwelling flux estimate, subject to our limited knowledge of r_s , ΔT_E , H_{ml} , and H_{tc} , and possibly to the vertical diffusional flux as well, which is ignored in this paper. A number of experiments have been performed with tunable parameters such as Π , r_s , and ΔT_E perturbed within a plausible range (not shown). The residual term changes magnitude and even in sign, when those parameters are varied one after another, but the analysis results critical to the major conclusions of this study are qualitatively insensitive to the perturbations imposed. The current findings would therefore be similar if the same analysis were repeated with an ideal dataset subject to no closure error. The shortwave and latent heat fluxes, having a predominant magnitude over other fluxes, are perhaps the main sources of the bias poleward of 10°S and 10°N . The residual term becomes nonnegligibly large near 20°S and 20°N , while our present interest is limited to latitudes lower than 15° where the ITCZ mostly stays.

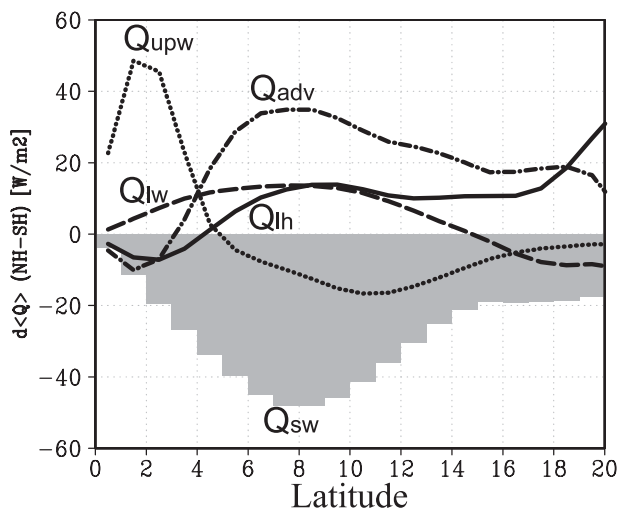


FIG. 3. North-south difference in climatological zonal-mean (125° – 100° W) heat fluxes computed for each latitude denoted by the abscissa. North exceeds south when the differential flux is positive. Plotted are absorbed shortwave flux (Q_{sw} , shaded histogram), latent heat flux (Q_{lh} , solid), upwelling heat flux (Q_{upw} , dotted), longwave flux (Q_{lw} , dashed), and advective heat flux (Q_{adv} , dotted-dashed).

The equatorial asymmetry is quantitatively demonstrated in Fig. 3, where the difference between the Northern and Southern Hemispheres is computed at each latitude for individual heat fluxes. The absorbed shortwave flux (shaded) has a negative asymmetry (i.e., the SEP flux exceeds the NEP flux) with the magnitude largest among all of the heat fluxes. In contrast, the advective, longwave, and latent heat fluxes show a positive asymmetry between 5° and 15° in latitude. Although it is least significant when compared in absolute value (Fig. 2b), the advective heat flux has the largest equatorial asymmetry among these three fluxes and is therefore the most important heat-budget component that counteracts the asymmetry exerted by the absorbed shortwave flux. The upwelling heat flux dominates the narrow equatorial area at latitudes lower than 5° , beyond which the upwelling cooling rapidly tapers off. Given that the latitude at 5° meridionally separates the ITCZ from the equatorial cold tongue, it is suggested that, while the advective heat flux may play a crucial role in the ITCZ asymmetry, the contribution of upwelling cooling is limited to the equatorial cold tongue.

b. Factors controlling the shortwave modulation

The meridional modulation of absorbed shortwave flux is ascribable to multiple factors including high and low cloud fractions and mixed layer absorptivity. Figures 4a–c show the climatological maps of total cloudiness and its decomposition into high and low cloud fractions. The geographical distribution of the high cloud fraction is

clearly delineated in the northern ITCZ region, while the low cloud fraction is enhanced over cold oceans where maritime stratocumuli often develop. Note that the HERB product uses passive microwave and visible-infrared measurements and therefore identifies both high and low clouds even where they coexist.

The large-scale variability of the BOA shortwave flux (Fig. 4d) is apparently explained by the shielding effects of high clouds extending along the north ITCZ as well as stratocumulus cloud decks. The spatial pattern of the shortwave flux is slightly modulated when multiplied by the mixed layer absorptivity (Fig. 4e), leading to a further reduction of the absorbed shortwave flux around 5° – 10° N, as seen in Fig. 2a, due to a systematic northward decrease of the mixed layer absorptivity [Fig. 4f, see also Fig. A2 in Masunaga and L'Ecuyer (2010) for the spatial distribution of the mixed layer depth].

Although the conspicuous shortwave reduction in the ITCZ has been long recognized (Oberhuber 1988; Mitchell and Wallace 1992; Cronin et al. 2006), high clouds extending along the ITCZ are often considered more as a result of the ITCZ asymmetry and less as a cause for it. The ITCZ clouds, however, appear to play a key role in the shortwave modulation for the study area of the present work. Since high clouds in the ITCZ are mainly associated with deep convection, their radiative impact is not just an external forcing to the mixed layer heat budget but relies on the preexisting ITCZ, suggesting the presence of feedback processes that maintain the observed equatorial asymmetry.

c. Factors controlling the latent heat flux

The latent heat flux given by (2) may be decomposed into the scalar wind speed, $|\mathbf{u}_{10}|$, and the air-sea humidity difference, $[q_v^*(T_s) - q_v]$, as principal parameters responsible for its variability. These two components are separately plotted in Fig. 5. The zonal-mean wind speed and humidity difference are both double peaked, straddling an equatorial minimum and paralleling the meridional structure of the latent heat flux itself (Fig. 2b). The spatial variability of the air-sea humidity difference (Fig. 5b) is controlled mainly by the saturation vapor term $q_v^*(T_s)$, as inferred from the resemblance to the SST distribution (Fig. 1). The wind field in the study area consists of the southern and northern trades, which eventually converge into the ITCZ (Fig. 5b). The southeasterly, cross-equatorial trade decelerates as it approaches the equator, giving rise to the aforementioned wind minimum, before accelerating again beyond the equator (Wallace et al. 1989; Liu and Xie 2002).

Despite their mutual resemblance in the meridional pattern, the zonal-mean wind speed and humidity difference exhibit a subtle equatorial asymmetry in opposing

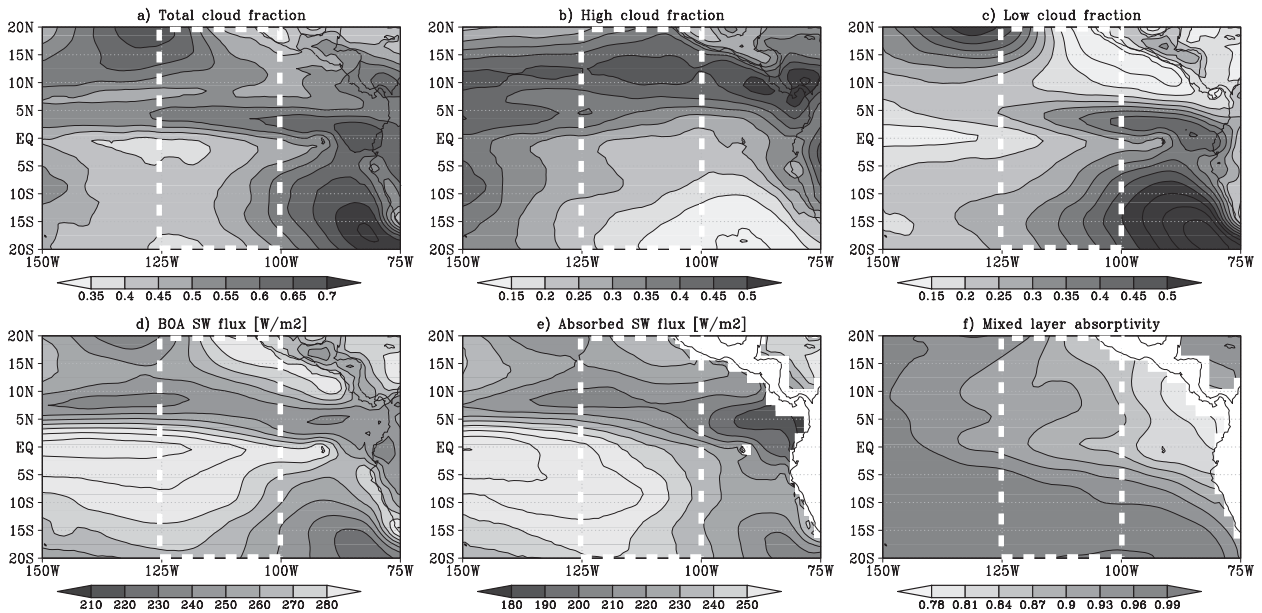


FIG. 4. Climatologies of (a) total cloudiness, (b) high cloud fraction, (c) low cloud fraction, (d) BOA shortwave flux (W m^{-2}), (e) absorbed shortwave flux (W m^{-2}), and (f) mixed layer absorptivity (Π). A darker shade corresponds to a smaller shortwave flux in (d) and (e), so shortwave flux is better compared with cloudiness in (a)–(c). The study area is indicated by the dashed box.

ways. The northern peak is slightly stronger than the southern peak in the air–sea humidity difference, while this asymmetry is reversed for the wind speed. Both effects are likely to arise from the presence of the north ITCZ where SST is higher (and thus the air–sea humidity difference larger) and the surface wind is weaker than on the opposite side of the equator. When combined into the latent heat flux, the wind speed asymmetry dominates that due to air–sea humidity.

The dynamics governing the surface wind over the tropical east Pacific was discussed by Xie and Philander (1994) in the context of explaining the ITCZ asymmetry. In a hypothesis later called the WES feedback, a sea level pressure gradient induced by the north ITCZ arguably enhances the wind speed in the SEP as the result of a southerly wind with a westward veer superposed on the background easterly trade. Observational evidence for the wind–ITCZ correlation is sought in month-to-month

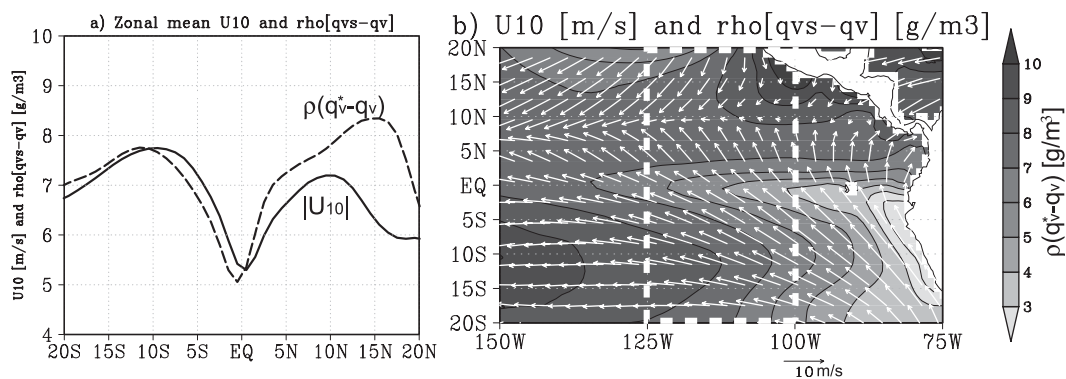


FIG. 5. (a) Climatological zonal-mean (125° – 100° W) scalar wind speed (m s^{-1}) ($|\mathbf{u}_{10}|$, solid) and air–sea humidity difference (g m^{-3}) ($\rho_a(q_s^* - q_v)$, dashed). Note that the humidity difference is defined with the dry-air density, ρ_a , multiplied. (b) Climatological 10-m wind vector and air–sea humidity difference contoured every 0.5 g m^{-3} . The study area for (a) is indicated by the dashed box. It should be noted that the climatological wind speed drawn in (a) is not $\langle |\mathbf{u}_{10}| \rangle$ but $\langle \mathbf{u}_{10} \rangle$, where the bracket designates the temporal mean, so that it does not necessarily agree with the norm of the wind vectors in (b).

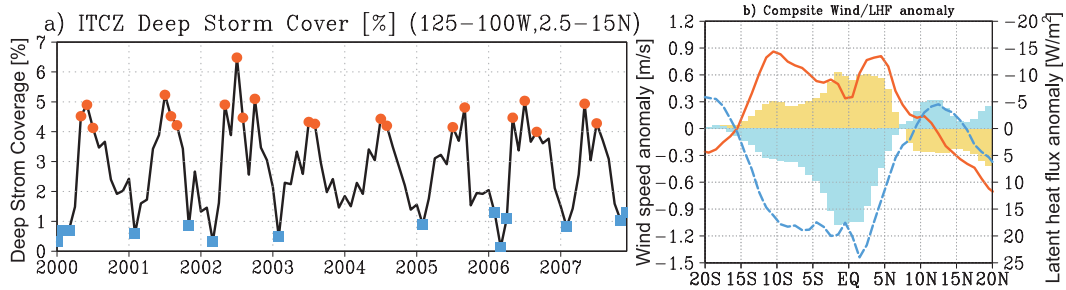


FIG. 6. (a) The time series of monthly mean deep storm coverage (%) for the north ITCZ region (2° – 15° N and 125° – 100° W). Red circles and blue squares indicate active months and inactive months, respectively, as defined by deviation from the mean with the one-sigma threshold. (b) Zonal-mean (125° – 100° W) wind speed (shaded histogram, labeled on left axis) and latent heat flux (lines, labeled on right, upside-down) anomalies for active months (yellow/red) and inactive months (blue).

variability shown in Fig. 6. The time series of deep storm coverage averaged over the NEP, as a proxy of the north ITCZ activity, exhibits a pronounced temporal (primarily seasonal) variation. Active (inactive) months can be defined as periods when deep storm coverage is larger (smaller) than the all-month mean (2.64) by at least one standard deviation (1.32). The zonal-mean wind speed and latent heat flux averaged for active/inactive months are plotted as anomalies from climatology in Fig. 6. It is clear that wind speed is enhanced in the SEP when the north ITCZ is active, while this pattern is almost precisely reversed when inactive. The latent heat flux closely follows this variation, deviating from the climatology by -15 or $+20 \text{ W m}^{-2}$ near 10° S. Although correlation does not necessarily imply causality, the wind speed probably responds to the ITCZ activity on a monthly mean basis. This result per se, however, does not guarantee that the WES feedback is entirely responsible for the ITCZ asymmetry, as will be discussed further in section 6.

d. Factors controlling the advective heat flux

Figure 7a shows, as found in Fig. 2b, that the advective heat flux has a notable meridional asymmetry characterized by a positive heat flux in the ITCZ and to its north. To isolate the origins of this pattern, the advective heat flux is broken down into SST and current velocity in Fig. 7b. A negative advective heat transport dominating the SEP and equatorial band is obviously brought by the South Equatorial Current carrying cold water to the west from near the South American coast and equatorial cold tongue. An area of positive heat transport north of 7° N is somewhat more complicated to interpret. In an attempt to clarify its origins, the easterly and westerly conditioned composites of advective heat flux and current velocity are individually plotted in Fig. 8, where days with a negative (positive) zonal current are isolated to construct the easterly (westerly) conditioned composite. Note that the advective flux composites, each weighted by the number

of days sampled, add up to the total (unconditional) mean (i.e., Fig. 7a) when summed together. The easterly conditioned composite (Fig. 8a) shows a broad patch of positive advective heat flux over the NEP, ascribable to the North Equatorial Current (NEC) carrying warm water from an area of high SST offshore from Central America, or the eastern Pacific warm pool. When conditioned by the westerly current, on the other hand, the advective heat flux is more neutral but makes a small contribution to the positive heat transport north of 5° N, fed by the

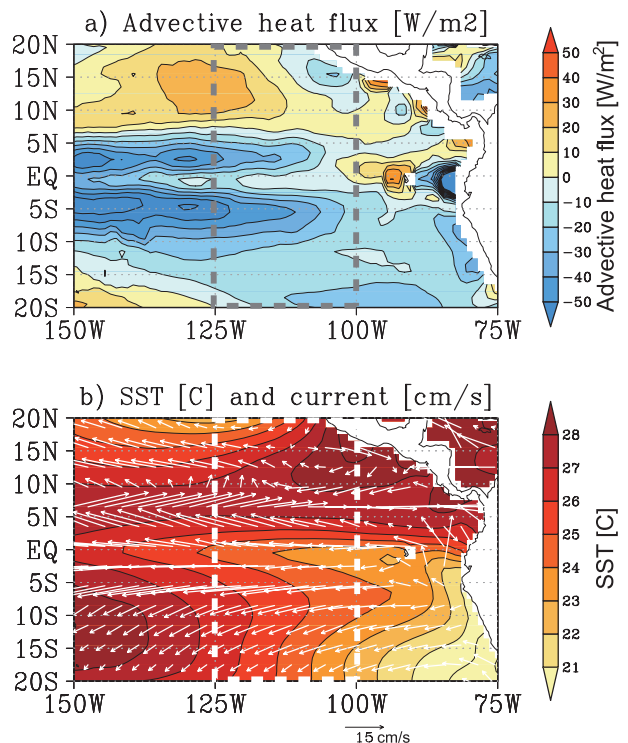


FIG. 7. Climatologies of (a) advective heat flux (W m^{-2}) and (b) SST ($^{\circ}\text{C}$) (colored) overlaid with ocean current velocity (cm s^{-1}). The study area is indicated by the dashed box.

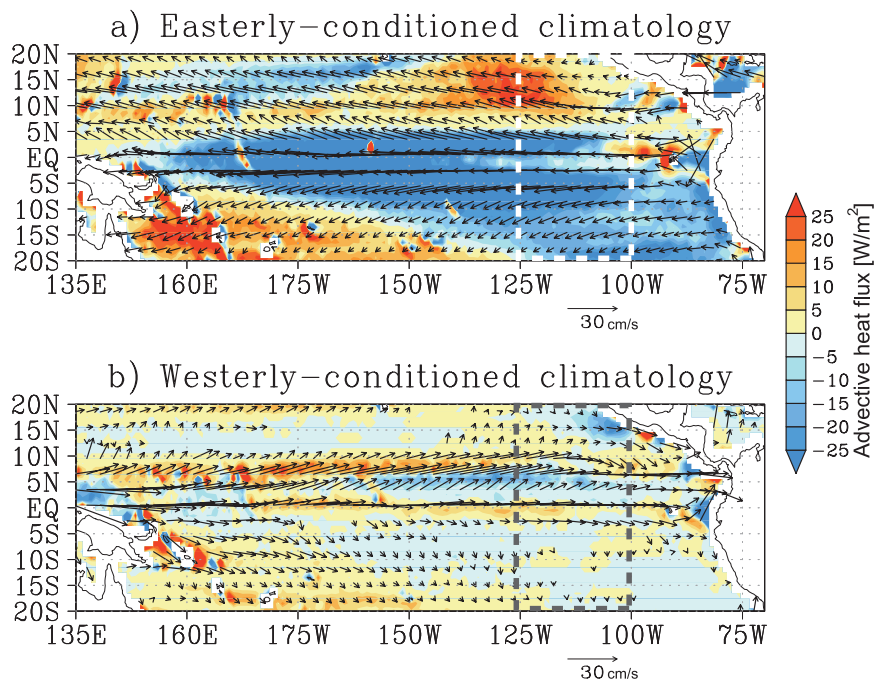


FIG. 8. Composite advective heat flux (W m^{-2}) and current velocity (cm s^{-1}) conditioned by (a) easterly and (b) westerly currents. See text for the procedure of the conditional averages. The study area is indicated by the dashed box.

North Equatorial Counter Current (NECC) that flows along the ITCZ. As such, the warm water advection in the northeast Pacific comprises two separate sources: one originating in the east Pacific warm pool through the NEC and, to a lesser extent, another linked with the west/central Pacific ITCZ through the NECC.

We are now left with two questions to address in order to understand the root of the meridional asymmetry in the advective heat flux. The first is why the east Pacific warm pool exists only in the NEP, and the other is why the SEP lacks a band of westerly current as the NECC. The first question requires an explanation for the mechanisms maintaining the east Pacific warm pool. The meteorology of the wind specific to this area is of critical importance among processes governing the SST (Xie et al. 2005), and therefore the ocean heat budget there is sensitive to topographical constraints including continental geography and local orography that directly dictate the wind and coastal current. The geographical configuration of the landmass is highly asymmetric at the eastern end of the tropical Pacific, and has been found by coupled model experiments to impose a strong constraint on the ITCZ asymmetry (Philander et al. 1996; Xie and Saito 2001). The second question is rather a classical problem belonging to Sverdrup's theory. The equatorial doldrums in the ITCZ are ultimately responsible for the NECC underneath as a result of a negative (positive) wind stress

curl induced to its south (north). It follows that the absence of a southern counterpart of the NECC is attributed to the fact that the SEP has no permanent ITCZ.

4. Austral fall climatology and double ITCZ

Potential causes for the equatorial asymmetry in individual heat fluxes were discussed in some detail in the previous section. High cloudiness associated with deep convection has the greatest influence on the shortwave modulation in the ITCZ. The surface wind is the principal element controlling the latent heat flux and shows a month-to-month variation closely related to the ITCZ activity. The meridional asymmetry in advective heat flux is sustained by a heat transport by the NEC and another by the NECC. Whereas geographic origins presumably account for the fact that the NEC is fed with warm water and the SEC with cold, all other factors mentioned above require a preexisting asymmetry of the ITCZ. If the ITCZ were on both sides of the equator in the first place, one might expect that the resultant fields of high cloudiness, wind speed, and equatorial counter current would be symmetric as well, being in balance rather than driving toward the asymmetric state observed. Indeed, Fig. 6 implies that the wind reduction in the SEP for the months of an inactive ITCZ is large enough to offset the climatological equatorial asymmetry of latent heat flux.

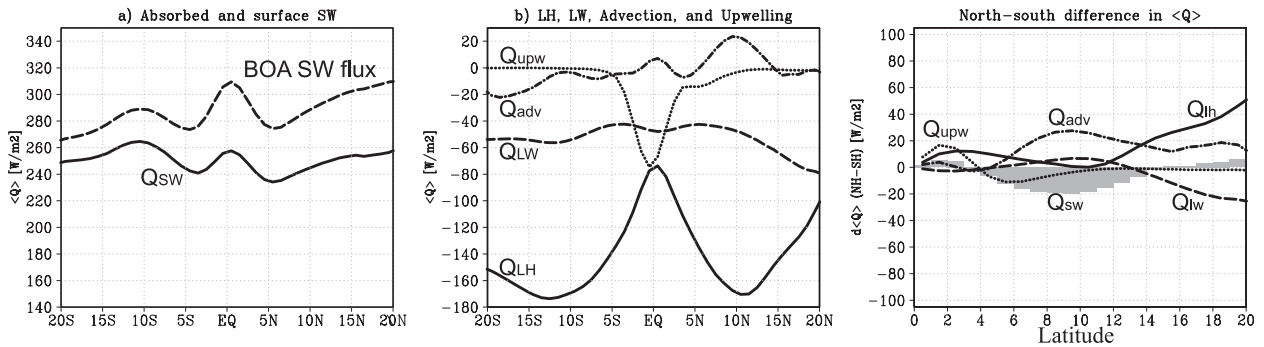


FIG. 9. (a),(b) As in Figs. 2a,b but for the bimonthly climatology for March and April. (c) As in Fig. 3 but for the bimonthly climatology for March and April.

This hypothetical symmetric condition may be exemplified by the *seasonal* double ITCZ that appears in austral fall, as seen in Fig. 1b (Masunaga and L'Ecuyer 2010, and references therein). Figure 9 shows the March–April bimonthly climatology of zonal-mean heat fluxes as in Fig. 2. The BOA shortwave flux exhibits paired minima symmetrically aligned at 5°S and 5°N, according to the latitudinal location of the ITCZ in this season. This symmetry is slightly skewed when absorbed into the ocean mixed layer as a result of the north–south gradient of mixed layer absorptivity. The latent heat flux is also symmetric about the equator within latitudes containing the ITCZ (~10°S–10°N). In contrast, the advective heat flux retains some asymmetry, as seen in the annual mean field, with a distinct positive peak associated only with the north ITCZ. Figure 10a presents the advective heat flux averaged for March and April. Unlike the annual mean field shown in Fig. 7a, a positive heat transport is evident off the South American coast, arising from the SEP warm band observed only in this season (Fig. 10b, see also Masunaga and L'Ecuyer 2010). This warm water transport, however, is not as efficient as is in the NEP, presumably owing to the transience of the south ITCZ as well as to the absence of a prominent warm pool in the SEP. There is also no recognizable South Equatorial Counter Current (SECC) despite the presence of a double ITCZ at this time of year. If a SECC existed, it could supply the south ITCZ with warm water across a large SST gradient in the SPCZ and enhance the advective heat flux in the SEP, making its zonal mean profile more symmetric about the equator. This appears not to be the case because the south ITCZ does not persist long enough for ocean dynamics to attain Sverdrup equilibrium in response to the rapidly changing atmospheric forcing.

5. On the persistence of the north ITCZ

Masunaga and L'Ecuyer (2010) showed observational evidence demonstrating that the development

and disappearance of the south ITCZ are primarily controlled by the seasonal cycle of insolation. An outstanding question concerning the equatorial asymmetry of the ITCZ is what keeps the north ITCZ active throughout the year against the seasonally varying solar forcing. The seasonal cycle of heat flux forcing is examined next to address this problem.

a. Seasonal cycle

Figure 11 shows the climatological annual time series of ocean surface heat fluxes averaged over the SEP and NEP individually. The residual in the annual mean flux

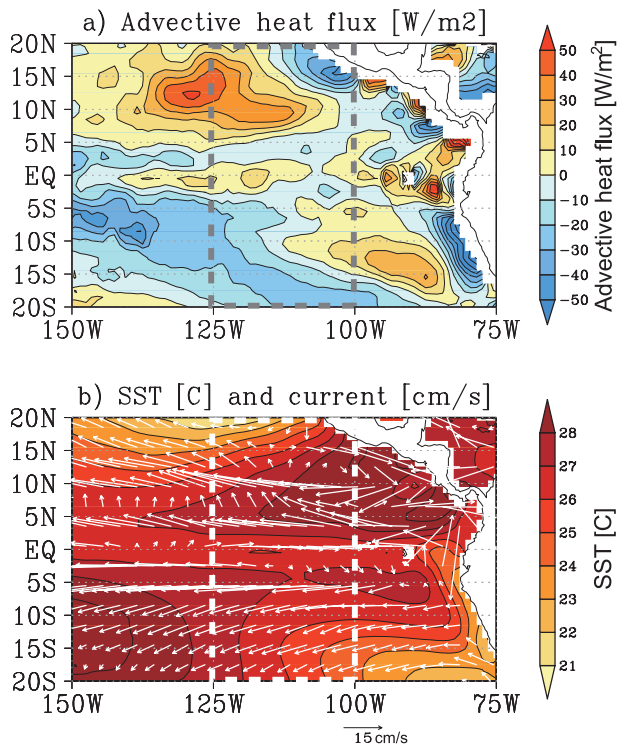


FIG. 10. As in Fig. 7 but for the bimonthly climatology for March and April.

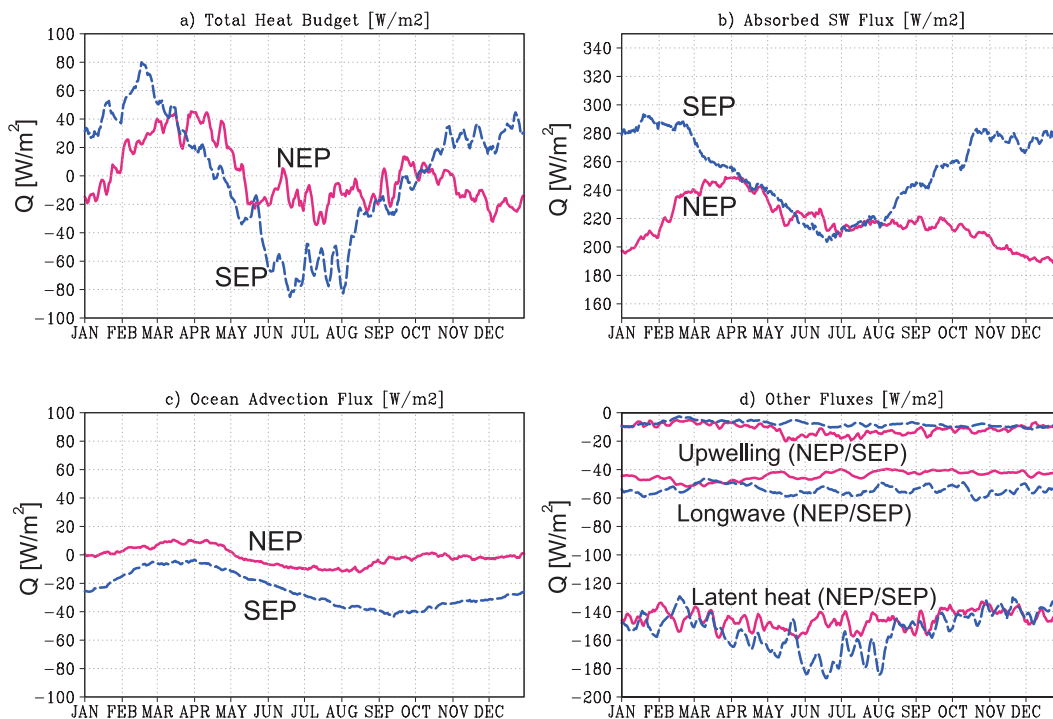


FIG. 11. Climatological annual time series of (a) net heat flux (with the residual term subtracted), (b) absorbed shortwave flux, (c) advective heat flux, and (d) upwelling, longwave, and latent heat fluxes as indicated. The NEP (2°N – 15°N , 125° – 100°W) and SEP (15° – 2°S , 125° – 100°W) are designated by solid-red and dashed-blue curves, respectively. The vertical axis spans 200 W m^{-2} for all panels.

has been subtracted from the net heat flux (Fig. 11a) to remove the offset. For the net heat flux, the SEP has a distinct annual cycle that is larger in amplitude and more sinusoidal in shape than in the NEP. Similar north–south contrast is also found in the absorbed shortwave flux (Fig. 11b). The absorbed shortwave flux stays smaller in the NEP than in the SEP, as found in section 3b. While the SEP is exposed to a well-defined annual cycle of shortwave flux, as readily expected from the seasonal migration of insolation, seasonality is rather muted in the NEP. Reasons for this contrast will be discussed shortly. Although the sinusoidal seasonality of the SEP shortwave flux resembles the net heat flux shown in Fig. 11a, the absorbed shortwave flux only accounts for approximately half of the amplitude. The other half can be attributed to other heat fluxes, among which the advective heat flux appears to have the largest amplitude of seasonal cycle (Fig. 11c). The advective heat flux exhibits a clear annual cycle with an amplitude of $\sim 50 \text{ W m}^{-2}$ in the SEP and a slight phase delay relative to the shortwave flux. The advective heat flux in the SEP reaches a maximum from March through April when the SEP warm band develops (see section 4). The NEP shows a weaker but discernible annual cycle in advective heat flux, probably due to the seasonal meridional shift of the east Pacific warm pool

(Wang and Enfield 2001). The remaining heat fluxes, all shown in Fig. 11d, do not have a notable seasonal cycle, except that Q_{LH} in the SEP slightly varies seasonally, reaching its largest negative flux in austral winter.

The contrast in absorbed shortwave flux between the SEP and NEP stems from a combination of multiple effects. As illustrated in Fig. 12a, the clear-sky solar flux at the BOA, $F_{\text{SW}}^{\text{clr}}$, is almost equivalent on either side of the equator when shifted in time by a half year; however, the small but finite eccentricity of the terrestrial orbit leads to a smaller amplitude annual cycle in the NEP relative to the SEP. The earth passes through perihelion in boreal winter in the present-day orbit, reducing the northern seasonal cycle of insolation and amplifying the southern cycle to a small extent. This tiny difference in amplitude of the annual cycle is enhanced when the mixed layer absorptivity, increasing southward across the equator in the tropical east Pacific (Fig. 4f), is also considered. The resulting annual cycle of absorbed shortwave flux, evaluated in the absence of any cloud-shielding effects, has an amplitude nearly twice as large in the SEP than in the NEP.

The seasonal cycle is further modulated when clouds are included in the shortwave budget (Fig. 12b). In the NEP, the cloud shortwave impact, or the difference between the all-sky and (hypothetical) clear-sky shortwave

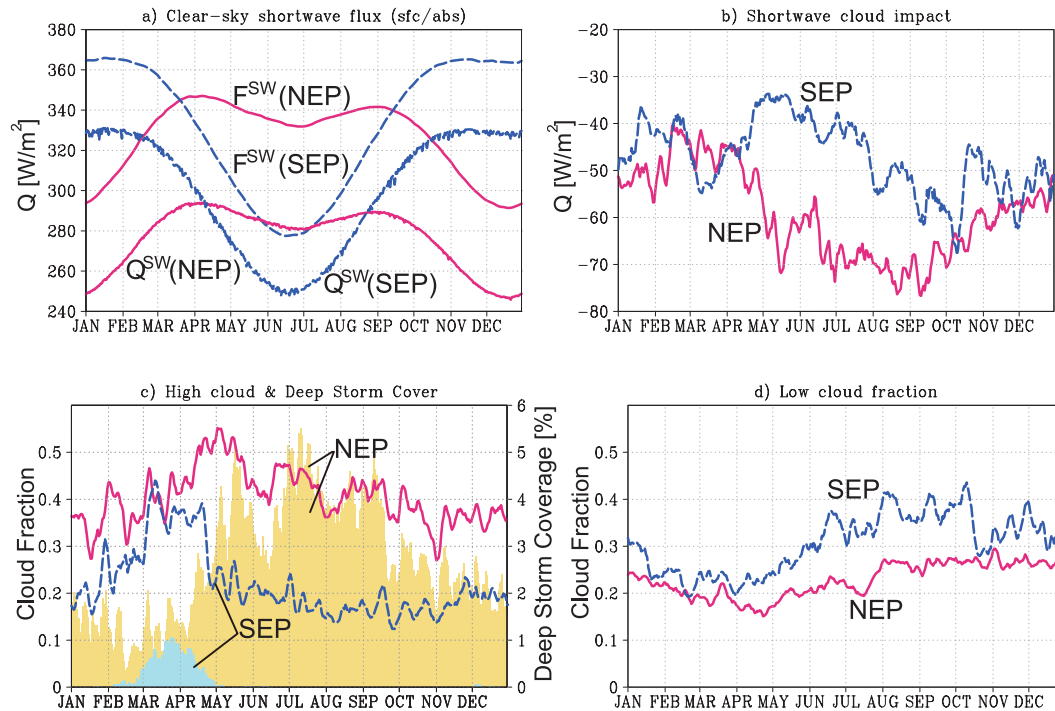


FIG. 12. Climatological annual time series of (a) clear-sky BOA shortwave flux (F_{SW}^{clr}) ($W m^{-2}$) and absorbed shortwave flux (Q_{SW}^{clr}) ($W m^{-2}$), (b) shortwave cloud impact ($Q_{SW} - Q_{SW}^{clr}$) ($W m^{-2}$), (c) high cloud fraction, labeled on left axis) and deep storm coverage (%) (shaded histogram, labeled on right), and (d) low cloud fraction. The NEP ($2^{\circ}N$ – $15^{\circ}N$, 125° – $100^{\circ}W$) and SEP (15° – $2^{\circ}S$, 125° – $100^{\circ}W$) are designated by solid–red and dashed–blue curves, respectively. The histogram is shaded in yellow (light blue) for the NEP (SEP).

fluxes, seasonally fluctuates between -40 (boreal winter) and $-70 W m^{-2}$ (summer). This variability is mainly controlled by the high cloud fraction, which stays large year round but moderately undulates loosely in phase with deep convective activity in the NEP (Fig. 12c). The high cloud variability there is nearly perfectly out of phase with the solar cycle, leading to a damping effect on the seasonality of absorbed shortwave flux in the NEP. Such a damping effect, on the other hand, is not expected for the SEP. Figure 12c shows that, since the period of active convection in the SEP is limited to austral fall, the high cloud fraction there drops by 50% throughout the remainder of the year. On the contrary, the low cloud fraction slightly increases from austral fall through winter in the SEP while remaining almost constant in the north. In summary, the north–south contrast in the annual cycle of clear-sky absorbed shortwave flux is somewhat enhanced when the cloud radiative impact is included, as the seasonal oscillation of cloudiness damps the shortwave variability in the NEP but not in the SEP.

b. Synthetic SST

The north–south difference in the annual cycle of the ocean surface heat flux is crucial for understanding

persistence of the north ITCZ. This is demonstrated in this section by the synthetic SST generated by the heat flux forcing estimated in this work. The overall strategy follows that outlined by Masunaga and L'Ecuyer (2010) with a few updates.

Three experiments were set up to compute the SST with the heat budget in Eq. (1), where all heat fluxes are given as the climatological annual time series. Beside the control experiment, a second experiment is carried out where the NEP flux, shifted in time by a half year, is mirrored onto the SEP; that is, $Q_{net}(x, y, t)$ is replaced by $Q_{net}(x, -y, t - T/2)$ for negative latitudes ($y < 0$), while Q_{net} remains unchanged in the NEP. Similarly, a third experiment is performed with the NEP flux replaced by the SEP flux with the phase adjusted. The second and third experiments, named the mirrored SEP and mirrored NEP experiments, respectively, are aimed at finding out how the north and south ITCZs are altered if the seasonal cycle of heat flux forcing is symmetric about the equator. All three of these experiments are initialized with the observed climatological SST on 1 January and integrated over time using a daily time step through the end of the year. The $\langle Q_{res} \rangle$ term on the rhs of (1) assures that the climatological SST should be annually periodic.

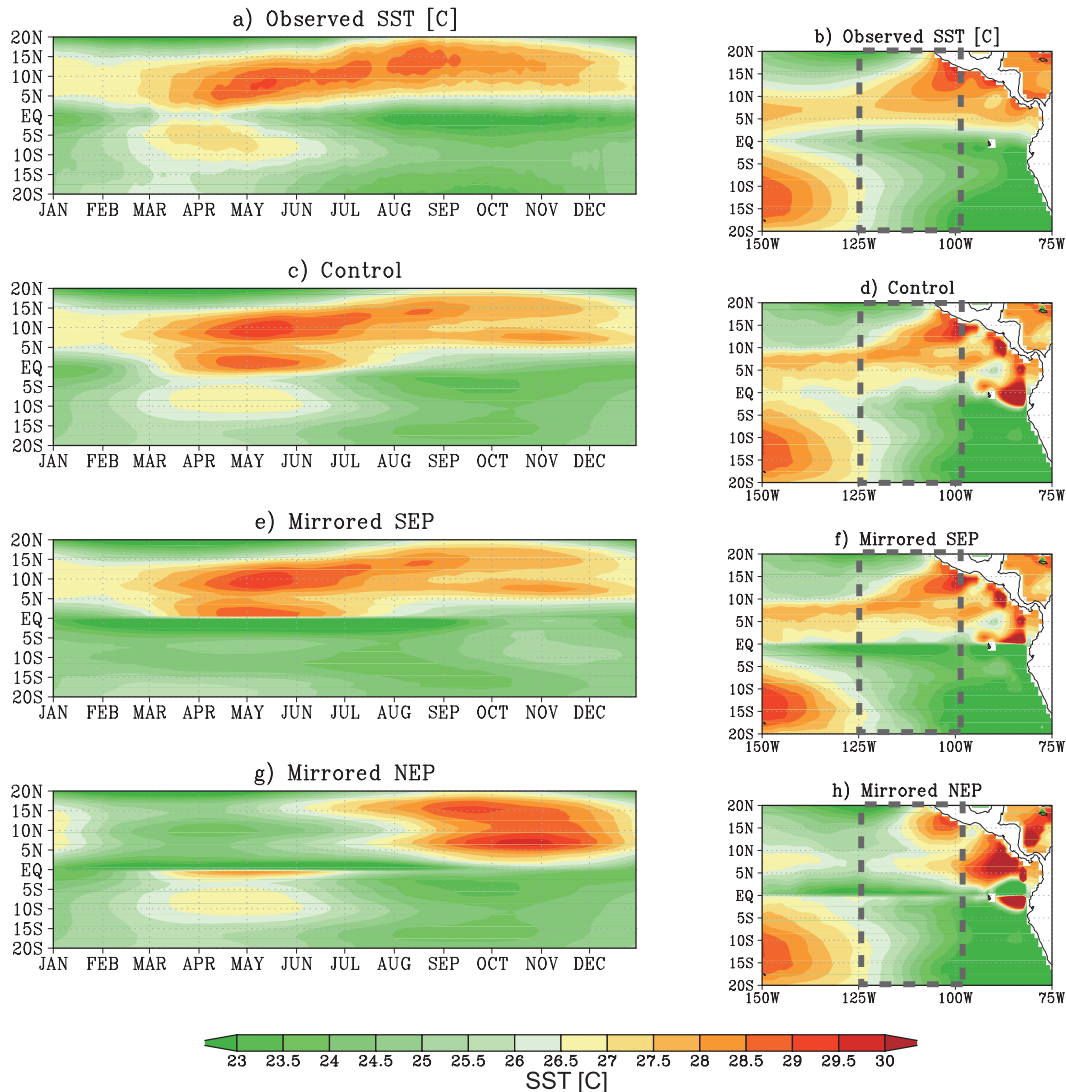


FIG. 13. (a) Climatological annual time series of observed SST ($^{\circ}\text{C}$) in the time–latitude domain averaged over 125° – 100°W and (b) annual climatology of observed SST ($^{\circ}\text{C}$). (c),(d) As in (a),(b) but for synthetic SST from the control experiment. (e),(f) As in (a),(b) but for synthetic SST from the mirrored SEP experiment. (g),(h) As in (a),(b) but for synthetic SST from the mirrored NEP experiment. See text for experimental design. The study area in (a),(c),(e), and (g) is indicated by the dashed box.

The experimental results are shown in Fig. 13 together with the observed SST for reference. The time–latitude section of observed SST (Fig. 13a) clearly delineates the persistent north ITCZ with a subtle seasonal north–south migration and the SEP warm band temporarily developing in austral fall. In the control experiment, shown in Fig. 13c, the north ITCZ is split into two bands from April to July. This artifact, arising in the vicinity of the equator, is probably due to the limited capability of estimating the upwelling heat flux, as noted in section 3a. Outside the equatorial band, the control experiment overall reproduces the observed properties. When averaged

over the year, the control experiment is reasonably close to the observed geographical SST distribution (Figs. 13b and 13d).

No sign for the austral fall double ITCZ is identifiable in the mirrored SEP experiment (Figs. 13e and 13f). Note that a 180° phase difference in the heat flux seasonality between the SEP and NEP resulted in an artificial discontinuity at the equator. In this experiment, the seasonal cycle of the net heat flux is weakened over the SEP and is no longer able to give rise to the SEP warm band. The meridional SST contrast introduced by the initial conditions is more or less preserved throughout the year in the

absence of a strong seasonal variation in heat flux forcing. In contrast, the mirrored NEP experiment provides a very different result. Synthetic SST from this experiment is now seasonally variable in the NEP as well as in the SEP, leading to a seasonally alternating ITCZ appearing on either side of the equator (Fig. 13g). The enhanced seasonality in the NEP no longer favors a persistent ITCZ. The SST in the NEP warms to 29°C in boreal fall but this warming is nearly canceled out when averaged over the year. The north ITCZ, as far as inferred from the synthetic SST, almost vanishes between January and August in the mirrored NEP experiment (Fig. 13h). Thus, it can be inferred that the persistence of the north ITCZ is largely caused by the damped seasonal cycle of the NEP heat flux forcing.

6. Discussion and conclusions

This paper addresses a long-standing problem with the equatorial asymmetry of the east Pacific ITCZ from the perspective of the ocean surface heat budget. While coupled model simulations have been successfully exploited by many previous studies relevant to this problem, the current analysis makes use of satellite measurements for evaluating the heat flux forcing to the ocean mixed layer. The annual mean climatology of the absorbed shortwave flux shows a prominent meridional asymmetry, marked with a 40 W m^{-2} difference between 10°S and 10°N, mainly due to shortwave reflection by high clouds associated with ITCZ convection. The mystery does not lie in what sustains the equatorial asymmetry against the annually symmetric solar forcing as is often claimed. A proper way to pose the problem is how the *asymmetric* shortwave forcing is counteracted by other heat fluxes in tandem and how the resulting heat flux distribution physically regulates the ITCZ structure, including a possible feedback to high cloud variability responding to ITCZ convection.

Xie and Seki (1997) analyzed the individual contributions of wind, humidity difference, cloudiness, and sea–air temperature difference to the ocean surface heat budget and concluded that the sun-shielding effect of high clouds is largely offset by high relative humidity in the equatorial asymmetry. They argued that the meridional asymmetry of wind is crucial for maintaining the observed north–south asymmetry of SST in the way that latent heat flux as a whole is locally balanced with the incoming radiative flux. An analysis similar to that of Xie and Seki (1997) is performed to see if the same conclusions are drawn from our surface flux estimates (Fig. 14). Figure 14 shows the equatorial asymmetry in latent heat flux and absorbed shortwave flux as in Fig. 3 and two additional hypothetical latent heat fluxes computed with each of the wind speed and humidity difference individually made symmetric about

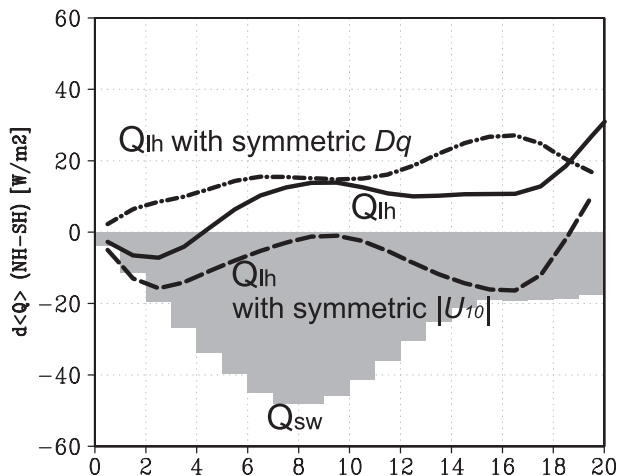


FIG. 14. North–south difference in climatological zonal-mean (125° – 100° W) latent heat and absorbed shortwave fluxes, computed for each latitude denoted by the abscissa. North exceeds south when the differential flux is positive. Plotted are latent heat flux (Q_{LH} , solid) as it is; Q_{LH} recomputed with an adjusted humidity difference; $\rho_a[q_v^*(T_s) - q_v]$, symmetric about the equator (dashed); and Q_{LH} recomputed with an adjusted wind speed symmetric about the equator (dotted–dashed). The shaded histogram shows the absorbed shortwave flux as in Fig. 3.

the equator in (2). The equatorial asymmetry in latent heat flux would be somewhat enhanced (reversed) if the humidity difference (wind speed) were symmetric, as one might expect from Fig. 5. The expected magnitude of the asymmetry in latent heat flux by perturbing the humidity difference and wind speed, however, is much too small to fully offset the north–south contrast in absorbed shortwave flux at ITCZ latitudes, unlike the findings of Xie and Seki (1997). The origins of the quantitative disagreement from this earlier work are unknown, but are possibly due to the fact that the Xie and Seki analysis relies on an empirical parameterization to evaluate shortwave flux rather than a direct heat flux estimate.

The asymmetric shortwave forcing is, in fact, balanced not by the latent heat flux alone but by the combined effects of several heat fluxes. Among those participating in the east Pacific heat budget, the advective heat flux makes a larger contribution to the equatorial asymmetry than all other fluxes except the shortwave flux. This may be a little surprising because the advective heat flux is least important in magnitude for the east Pacific heat budget as a whole. The annual mean advective heat flux changes sign to positive as latitude increases beyond 7°N, owing to the warm water transport from the east Pacific warm pool and, to a lesser extent, the NECC. The meridional asymmetry arises because the SEP has neither a warm pool nor an equatorial countercurrent to supply warm water. The latent heat flux, largest among the negative (or cooling) fluxes,

has a moderate asymmetry governed by the scalar wind speed that is somewhat larger in the SEP than in the NEP. The longwave flux is relatively homogeneous across the east Pacific. The upwelling heat flux is largest in both magnitude and asymmetry within a narrow equatorial band between 5°S and 5°N while it quickly diminishes poleward beyond 5°S/N. The wind–upwelling interaction that amplifies the equatorial asymmetry, as suggested by Mitchell and Wallace (1992) and Chang and Philander (1994), may be operating in this limited latitudinal range centered on the equator, but is unlikely to directly influence the whole ITCZ structure, as also pointed out by Xie (2004).

A key to understanding the ITCZ asymmetry lies in the north–south contrast of the seasonal cycle in combination with the annual mean field. The seasonal cycle of heat flux forcing is found to be muted in the NEP relative to the SEP. Three separate factors account for this difference: 1) annual fluctuation of the earth–sun distance, 2) meridional gradient in mixed layer absorptivity, and 3) seasonal variation of the cloud shortwave impact. The first factor was also pointed out by Wang and Wang (1999) but in a somewhat different context. The third point does not have as large an impact as the first two combined but has noteworthy implications. High cloudiness tends to increase as deep convection intensifies from a cold to a warmer season, masking, in part, the seasonality of the BOA shortwave flux in the NEP. This may be viewed as a seasonal analog of the thermostat feedback (Ramanathan and Collins 1991), although a close examination of the underlying mechanism is outside the scope of the present study. On the other hand, maritime stratocumuli, dominating the low cloud fraction over the SEP, prefer colder oceans and potentially reinforce the preexisting seasonal and spatial variations of SST, as suggested by Philander et al. (1996). Such a low cloud impact on the shortwave flux is found to exist in the SEP but not to an extent that would overwhelm the high cloud impact in either the annual mean or seasonal cycle. The main body of the southeast Pacific stratocumulus cloud deck is indeed east of the current study area, closer to the Peruvian coast (see Fig. 4d). The stratocumulus regulation of SST, if at work, may be a localized effect near the coast, but a cold SST there could affect a broader region far to the west through advection. The advective heat flux, a major ingredient of the equatorial asymmetry, originates from a remarkable contrast between the east Pacific warm pool in the north and a cloud-covered cold pool in the south providing a pathway for continental geography to impact the ITCZ asymmetry (Philander et al. 1996; Xie and Saito 2001). Regions under the direct influence of the north–south SST disparity caused by the combination of these geographical and stratocumulus effects

can be communicated by advective flux to the rest of the eastern Pacific basin.

The month-to-month variation of wind speed and latent heat flux in the SEP is found to be positively correlated with north ITCZ activity as expected from the WES feedback hypothesis. The WES feedback, on the other hand, is known to lose its control on the ITCZ asymmetry when exposed to a strong seasonal forcing (Xie 1996, 1997a). Since the asymmetric WES mode grows at a rate much slower than a seasonal time scale (Xie 1997b), the ability of the WES feedback to explain the observed ITCZ asymmetry is limited by the overwhelming seasonality of solar forcing. Xie (1996, 1997a) demonstrated that the east Pacific ITCZ would become more equatorially symmetric in the annual mean as the seasonal forcing strengthens, assuming that the amplitude of seasonal shortwave forcing is equal on both sides of the equator. In reality, however, the seasonal cycle of the absorbed shortwave flux has substantially different amplitudes between the Northern and Southern Hemispheres. As a result, the ITCZ retains its equatorial asymmetry because the magnitude of seasonal forcing is a critical element for the persistence or transience of the ITCZ.

A set of simple experiments were carried out to study the role of the seasonally varying heat flux forcing in the persistence of the north ITCZ. Modeled SST is found to be subject to a strong seasonal cycle in the north ITCZ if the NEP heat flux forcing is replaced by SEP values, leading to a significant weakening of the north ITCZ in the annual mean. Interestingly, the resultant seasonality when the north and south ITCZs emerge and disappear in turn is similar to the “seasonally alternating ITCZ error” inherent in some coupled climate models (de Szoeke and Xie 2008). The regional contrast in the seasonality of heat flux forcing might be one of the factors responsible for such model biases.

This paper is focused on the ocean mixed layer head budget and its potential impact on the atmospheric dynamics has yet to be examined further in depth. The current work needs to be extended to future studies with the complete circle of air–sea feedback considered to fully understand the interactive mechanisms sustaining the ITCZ. In addition, the heat budget analysis conducted here relies on many assumptions and simplifications that compensate relatively limited pieces of information available from satellite observations. The present results and implications would need verification by coupled ocean–atmosphere models of reasonable complexity and flexibility where the processes vital for the ITCZ asymmetry are individually tested. Such modeling studies exist but have more or less focused on assessing the effects of wind, upwelling, and low clouds with known hypotheses in mind, where some key processes such as advective heat flux have

been largely overlooked. Benchmark estimates of the heat fluxes and resulting cloud structure as provided by this study could be used to initialize and/or evaluate future climate model simulations, which would lead to a deeper understanding of the equatorial asymmetry of the east Pacific ITCZ.

Acknowledgments. The TRMM PR (2A25) and VIRS (1B01) datasets were provided by the Japan Aerospace Exploration Agency (JAXA) Earth Observation Research Center (EORC), and the TMI- and AMSR-E-retrieved SST and CWV datasets by the Remote Sensing Systems (information online at www.ssmi.com). The QuikSCAT SeaWinds ocean wind vector data and OSCAR surface current product were obtained from the Physical Oceanography Distributed Active Archive Center (PO.DAAC) at the NASA Jet Propulsion Laboratory, Pasadena, California (information online at podaac.jpl.nasa.gov). The AIRS level 3 daily gridded product was acquired as part of the activities of NASA's Science Mission Directorate, and is archived and distributed by the Goddard Earth Sciences (GES) Data and Information Services Center (DISC). The WOA05 temperature data were obtained from the NOAA/National Oceanographic Data Center. The mixed layer depth dataset was downloaded online (www.lodyc.jussieu.fr/~cdblod/mld.html). This work is supported by the Ministry of Education, Culture, Sports, Science, and Technology (MEXT) Grant-in-Aid for Young Scientists 20740269. The HERB dataset was generated under the support of National Aeronautics and Space Administration (NASA) Energy and Water Cycle Study (NEWS) Grant NAG06GC46G.

REFERENCES

- Bauer, S., M. S. Swenson, A. Griffa, A. J. Mariano, and K. Owens, 1998: Eddy-mean flow decomposition and eddy-diffusivity estimates in the tropical Pacific Ocean. *J. Geophys. Res.*, **103**, 30 855–30 871.
- Bonjean, F., and G. S. E. Lagerloef, 2002: Diagnostic model and analysis of the surface currents in the tropical Pacific Ocean. *J. Phys. Oceanogr.*, **32**, 2938–2954.
- Chang, P., 1994: A study of the seasonal cycle of sea surface temperature in the tropical Pacific Ocean using reduced gravity models. *J. Geophys. Res.*, **99**, 7725–7751.
- , and S. G. Philander, 1994: A coupled ocean–atmosphere instability of relevance to the seasonal cycle. *J. Atmos. Sci.*, **51**, 3627–3648.
- Cronin, M. F., N. A. Bond, C. W. Fairall, and R. A. Weller, 2006: Surface cloud forcing in the east Pacific stratus deck/cloud tongue/ITCZ complex. *J. Climate*, **19**, 392–409.
- Dai, A., 2006: Precipitation characteristics in 18 coupled climate models. *J. Climate*, **19**, 4605–4630.
- de Boyer Montégut, C., G. Madec, A. Fischer, A. Lazar, and D. Iudicone, 2004: Mixed layer depth over the global ocean: An examination of profile data and a profile-based climatology. *J. Geophys. Res.*, **109**, C12003, doi:10.1029/2004JC002378.
- de Szoek, S. P., and S.-P. Xie, 2008: The tropical eastern Pacific seasonal cycle: Assessment of errors and mechanisms in IPCC AR4 coupled ocean–atmosphere general circulation models. *J. Climate*, **21**, 2573–2590.
- Jin, Z., T. P. Charlock, W. L. S. Smith Jr., and K. Rutledge, 2004: A parameterization of ocean surface albedo. *Geophys. Res. Lett.*, **31**, L22301, doi:10.1029/2004GL021180.
- Kraus, E. B., and J. A. Businger, 1994: *Atmosphere–Ocean Interaction*. Oxford University Press, 362 pp.
- Kubota, M., N. Iwasaka, S. Kizu, M. Konda, and K. Kutsuwada, 2002: Japanese ocean flux data sets with use of remote sensing observations (J-OFURO). *J. Oceanogr.*, **58**, 213–225.
- Lagerloef, G. S. E., G. T. Mitchum, R. B. Lukas, and P. P. Niiler, 1999: Tropical Pacific near-surface currents estimated from altimeter, wind, and drifter data. *J. Geophys. Res.*, **104**, 23 313–23 326.
- Large, W. G., and S. G. Yeager, 2009: The global climatology of an interannually varying air–sea flux data set. *Climate Dyn.*, **33**, 341–364.
- , J. C. McWilliams, and S. C. Doney, 1994: Oceanic vertical mixing: A review and a model with a nonlocal boundary layer parameterization. *Rev. Geophys.*, **32**, 363–403.
- L'Ecuyer, T. S., and G. L. Stephens, 2003: The tropical oceanic energy budget from the TRMM perspective. Part I: Algorithm and uncertainties. *J. Climate*, **16**, 1967–1985.
- , and —, 2007: The tropical atmospheric energy budget from the TRMM perspective. Part II: Evaluating GCM representations of the sensitivity of 29 regional energy and water cycles to the 1998–99 ENSO cycle. *J. Climate*, **20**, 4548–4571.
- , and G. McGarragh, 2010: A 10-year climatology of tropical radiative heating and its vertical structure from TRMM observations. *J. Climate*, **23**, 519–541.
- Li, T., 1997: Air–sea interactions of relevance to the ITCZ: Analysis of coupled instabilities and experiments in a hybrid coupled GCM. *J. Atmos. Sci.*, **54**, 134–147.
- Liu, W. T., and X. Xie, 2002: Double intertropical convergence zones—A new look using scatterometer. *Geophys. Res. Lett.*, **29**, 2054, doi:10.1029/2002GL015431.
- Locarnini, R. A., A. V. Mishonov, J. I. Antonov, T. P. Boyer, and H. E. Garcia, 2006: *Temperature*. Vol. 1, *World Ocean Atlas 2005*, NOAA Atlas NESDIS, Vol. 61, 182 pp.
- Masunaga, H., and C. D. Kummerow, 2006: Observations of tropical precipitating clouds ranging from shallow to deep convective systems. *Geophys. Res. Lett.*, **33**, L16805, doi:10.1029/2006GL026547.
- , and T. S. L'Ecuyer, 2010: The southeast Pacific warm band and double ITCZ. *J. Climate*, **23**, 1189–1208.
- , —, and C. D. Kummerow, 2005: Variability in the characteristics of precipitation systems in the tropical Pacific. Part I: Spatial structure. *J. Climate*, **18**, 823–840.
- McPhaden, M. J., M. F. Cronin, and D. C. McClurg, 2008: Meridional structure of the seasonally varying mixed layer temperature balance in the eastern tropical Pacific. *J. Climate*, **21**, 3240–3260.
- Mechoso, C. R., and Coauthors, 1995: The seasonal cycle over the tropical Pacific in coupled ocean–atmosphere general circulation models. *Mon. Wea. Rev.*, **123**, 2825–2838.
- Mitchell, T. P., and J. M. Wallace, 1992: The annual cycle in equatorial convection and sea surface temperature. *J. Climate*, **5**, 1140–1156.
- Murtugudde, R., J. Beauchamp, C. R. McClain, M. Lewis, and A. J. Busalacchi, 2002: Effects of penetrative radiation on the upper tropical ocean circulation. *J. Climate*, **15**, 470–486.
- Oberhuber, J. M., 1988: An atlas based on the 'COADS' data set: The budgets of heat, buoyancy and turbulent kinetic energy at the surface of the global ocean. Max Planck Institute for Meteorology Rep. 15, 20 pp.

- Philander, S. G. H., D. Gu, D. Halpern, G. Lambert, N.-C. Lau, T. Li, and R. C. Pacanowski, 1996: Why the ITCZ is mostly north of the equator. *J. Climate*, **9**, 2958–2972.
- Ramanathan, V., and W. Collins, 1991: Thermodynamic regulation of ocean warming by cirrus clouds deduced from observations of the 1987 El Niño. *Nature*, **351**, 27–32.
- Raymond, D. J., and Coauthors, 2004: EPIC 2001 and the coupled ocean–atmosphere system of the tropical east Pacific. *Bull. Amer. Meteor. Soc.*, **85**, 1341–1354.
- Stevenson, J. W., and P. P. Niiler, 1983: Upper ocean heat budget during the Hawaii-to-Tahiti Shuttle Experiment. *J. Phys. Oceanogr.*, **13**, 1894–1907.
- Swenson, M. S., and D. V. Hansen, 1999: Tropical Pacific Ocean mixed layer heat budget: The Pacific cold tongue. *J. Phys. Oceanogr.*, **29**, 29–81.
- Wallace, J. M., T. P. Mitchell, and C. Deser, 1989: The influence of sea-surface temperature on surface wind in the eastern equatorial Pacific: Seasonal and interannual variability. *J. Climate*, **2**, 1492–1499.
- Wang, B., and Y. Wang, 1999: Dynamics of the ITCZ–equatorial cold tongue complex and causes of the latitudinal climate asymmetry. *J. Climate*, **12**, 1830–1847.
- Wang, C., and D. B. Enfield, 2001: The tropical Western Hemisphere warm pool. *Geophys. Res. Lett.*, **28**, 1635–1638.
- Wang, W., and M. J. McPhaden, 1999: The surface layer heat balance in the equatorial Pacific Ocean. Part I: Mean seasonal cycle. *J. Phys. Oceanogr.*, **29**, 1812–1831.
- Wijesekera, H. W., D. L. Rudnick, C. A. Paulson, S. D. Pierce, W. S. Pegau, J. Mickett, and M. C. Gregg, 2005: Upper ocean heat and freshwater budgets in the eastern Pacific warm pool. *J. Geophys. Res.*, **110**, C08004, doi:10.1029/2004JC002511.
- Xie, S.-P., 1996: Effects of seasonal solar forcing on latitudinal asymmetry of the ITCZ. *J. Climate*, **9**, 2945–2950.
- , 1997a: Stability of equatorially symmetric and asymmetric climates under annual solar forcing. *Quart. J. Roy. Meteor. Soc.*, **123**, 1359–1375.
- , 1997b: Unstable transition of the tropical climate to an equatorially asymmetric state in a coupled ocean–atmosphere model. *Mon. Wea. Rev.*, **125**, 667–679.
- , 2004: The shape of continents, air–sea interaction, and the rising branch of the Hadley circulation. *The Hadley Circulation: Present, Past and Future*, H. F. Diaz and R. S. Bradley, Eds., Kluwer Academic, 121–152.
- , and S. G. H. Philander, 1994: A coupled ocean–atmosphere model of relevance to the ITCZ in the eastern Pacific. *Tellus*, **46A**, 340–350.
- , and M. Seki, 1997: Causes of equatorial asymmetry in sea surface temperature over the eastern Pacific. *Geophys. Res. Lett.*, **24**, 2581–2584.
- , and K. Saito, 2001: Formation and variability of a northerly ITCZ in a hybrid coupled AGCM: Continental forcing and oceanic–atmospheric feedback. *J. Climate*, **14**, 1262–1276.
- , H. Xu, W. S. Kessler, and M. Nonaka, 2005: Air–sea interaction over the eastern Pacific warm pool: Gap winds, thermocline dome, and atmospheric convection. *J. Climate*, **18**, 5–20.
- Zebiak, S. E., and M. A. Cane, 1987: A model El Niño–Southern Oscillation. *Mon. Wea. Rev.*, **115**, 2262–2278.